

Observing the quantum Mpemba effect in quantum simulations

Lata Kh Joshi,^{1, 2, 3} Johannes Franke,^{1, 4} Aniket Rath,⁵ Filiberto Ares,³
 Sara Murciano,⁶ Florian Kranzl,^{1, 4} Rainer Blatt,^{1, 4} Peter Zoller,^{1, 2} Benoît
 Vermersch,^{1, 2, 5} Pasquale Calabrese,^{3, 7} Christian F. Roos,^{1, 4} and Manoj K. Joshi^{1, 4, *}

¹*Institute for Quantum Optics and Quantum Information, Austrian
 Academy of Sciences, Technikerstraße 21a, 6020 Innsbruck, Austria*

²*University of Innsbruck, Institute for Theoretical Physics, Technikerstraße 21a, 6020 Innsbruck, Austria*

³*SISSA and INFN, via Bonomea 265, 34136 Trieste, Italy*

⁴*University of Innsbruck, Institute for Experimental Physics, Technikerstraße 25, 6020 Innsbruck, Austria*

⁵*Univ. Grenoble Alpes, CNRS, LPMMC, 38000 Grenoble, France*

⁶*Walter Burke Institute for Theoretical Physics, and Department of Physics and IQIM, Caltech, Pasadena, CA 91125, USA*

⁷*International Centre for Theoretical Physics (ICTP), Strada Costiera 11, 34151 Trieste, Italy*

The non-equilibrium physics of many-body quantum systems harbors various unconventional phenomena. In this study, we experimentally investigate one of the most puzzling of these phenomena—the quantum Mpemba effect, where a tilted ferromagnet restores its symmetry more rapidly when it is farther from the symmetric state compared to when it is closer. We present the first experimental evidence of the occurrence of this effect in a trapped-ion quantum simulator. The symmetry breaking and restoration are monitored through entanglement asymmetry, probed via randomized measurements, and post-processed using the classical shadows technique. Our findings are further substantiated by measuring the Frobenius distance between the experimental state and the stationary thermal symmetric theoretical state, offering direct evidence of subsystem thermalization.

I. INTRODUCTION

When a system is brought out of equilibrium, it may exhibit phenomena that defy conventional wisdom. One particularly puzzling example is the Mpemba effect, firstly described as the phenomenon where hot water freezes faster than cold water [1], and then extended to a wide variety of systems [2–8]. An anomalous relaxation, reminiscent of the Mpemba effect, can manifest at zero temperature in isolated many-body quantum systems. Specifically, starting from a configuration that breaks a symmetry, its restoration can happen more rapidly when the initial state shows a greater degree of symmetry breaking [9]. This behavior, dubbed as *quantum Mpemba effect* (QMPE), is driven by entanglement and quantum fluctuations. The origin and ubiquity of the QMPE are active areas of research. For instance, in integrable systems, the conditions under which the QMPE occurs are now well understood [10]. However, the existence of this effect remains outstanding in generic quantum systems—such as non-integrable and synthetic quantum many-body systems. In this regard, we experimentally explore the QMPE in a chain of spins interacting via power-law decaying interactions.

Present-day programmable quantum simulators, with their impeccable ability to create, manipulate, and analyze quantum states, provide us with excellent test beds to examine non-equilibrium dynamics in many-body quantum systems [11–14]. To address our objective of investigating the QMPE, we employ a trapped-ion quantum simulator consisting of $N = 12$ interacting spin-1/2 particles. The system is initialized into a product

state where each spin points in the z direction and subsequently all spins are tilted by an angle θ from the z axis. The spin states designated by $\theta = 0$ and π (we will refer to them as ferromagnetic states) are $U(1)$ symmetric as they remain invariant under a rotation about the z axis; conversely for $0 < \theta < \pi$ (tilted ferromagnets), the states explicitly break such symmetry. The tilted ferromagnetic state is then evolved with the engineered XY Hamiltonian [15–17] that also possesses the $U(1)$ symmetry and determines the properties of time-evolved states. The $U(1)$ symmetry implies the conservation of the magnetization in the z axis, i.e. the conserved charge is defined as $Q = 1/2 \sum_j \sigma_j^z$. In the thermodynamic limit, the reduced density matrix of a subsystem relaxes to a Gibbs ensemble [18–20], and the initially broken symmetry is restored [9]. The latter is a direct consequence of the Mermin-Wagner theorem which forbids spontaneous breaking of a continuous symmetry in 1D systems at finite temperatures [21, 22].

To set up an experimental indicator of symmetry-breaking, we consider a bipartition of the system as $A \cup \bar{A}$. The charge Q that generates the $U(1)$ symmetry decomposes into the contribution of each subsystem, i.e. $Q = Q_A + Q_{\bar{A}}$. The possible values q of the subsystem charge Q_A define the charge sectors. When a reduced density matrix is symmetric, it is block diagonal in the eigenbasis of Q_A . Based on this property, the restoration of the symmetry, at the level of a subsystem A , is estimated by the “Entanglement Asymmetry” (EA), defined as [9],

$$EA = \log[\text{Tr}(\rho_A^2)] - \log[\text{Tr}(\rho_{A,Q}^2)], \quad (1)$$

where $\rho_{A,Q}$ denotes the symmetrized counterpart of ρ_A i.e. $\rho_{A,Q} = \sum_{q \in \mathbb{Z}} \Pi_q \rho_A \Pi_q$. Each Π_q is the projector onto the charge sector q in the subsystem A . The EA is a non-

* manoj.joshi@uibk.ac.at

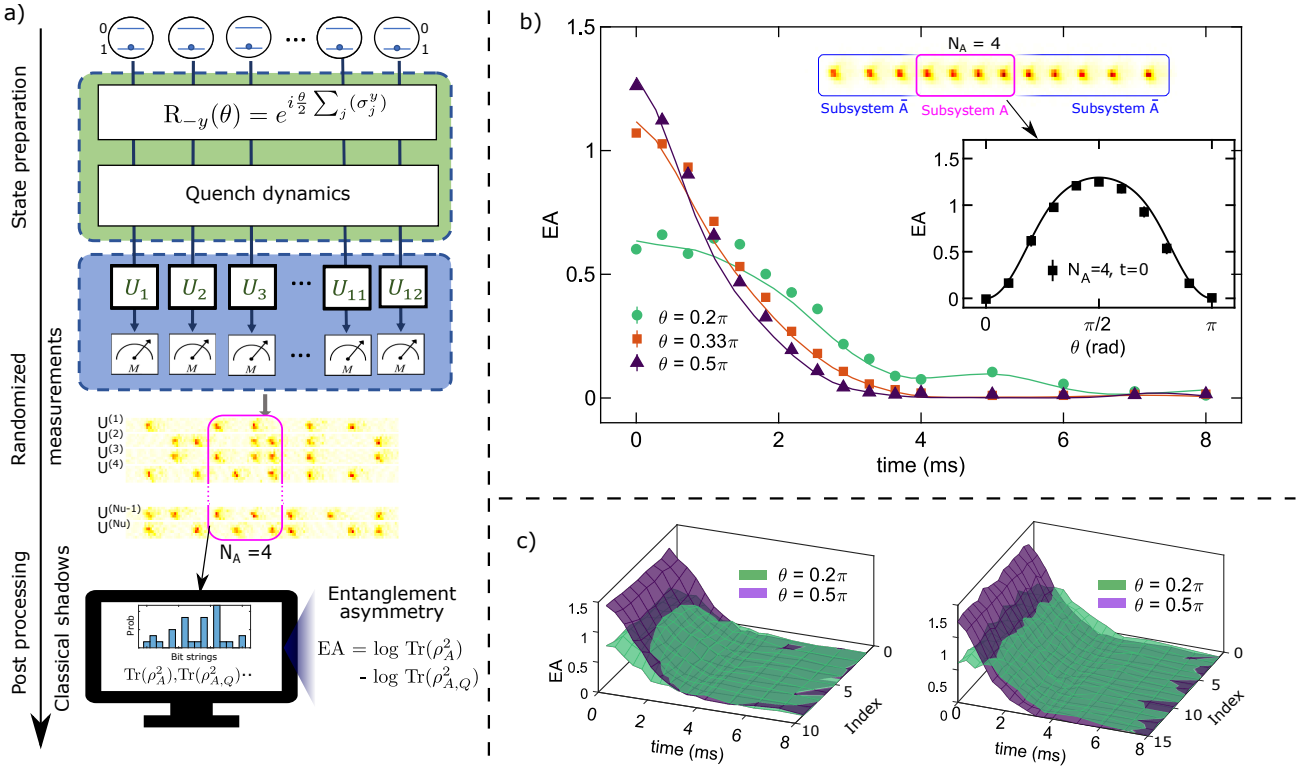


FIG. 1: **Measurement of the entanglement asymmetry (EA) with a 12 ion chain:** a) Protocol to measure the EA with a 1d array of 12 trapped ions using randomized measurements. After rotating the initially prepared ferromagnetic state by an angle θ , the system is evolved with the Hamiltonian of interest. After a time t , randomized local rotations and projective measurements are performed. The obtained bitstrings (constructed from site-resolved fluorescence images) are then classically processed to estimate the EA. b) Experimentally measured EA, averaged over all possible subsystems of size $N_A = 4$ chosen from ion indices between 4 and 9, is plotted for angles $\theta = 0.2\pi, 0.33\pi$ and 0.5π . A fast restoration of symmetry is observed for the largest angle, confirming the quantum Mpemba effect (QMPE). Inset presents the EA at initial time $t = 0$ as a function of the tilt angle θ . Solid curves denote theory and symbols are experimental data. Error bars are smaller than symbols. c) Experimentally measured EA for connected 4-qubit subsystems selected from the whole chain (on the left) and all possible 4-qubit subsystems (connected and disconnected) between ion numbers 4 to 9 (right) shows subsystem independence of the QMPE. The x axis represents the subsystem index detailed in the main text.

negative quantity that vanishes if and only if ρ_A is symmetric, that is $\rho_A = \rho_{A,Q}$ [9]. The EA has proven to be an effective tool for investigating broken symmetries, not only in out-of-equilibrium many-body systems [10, 23] but also in quantum field theories [24–26] and black hole physics [27]. For present studies, both parts of the above equation can be estimated using the classical shadow formalism from randomized measurements [28, 29].

In the current context, the QMPE manifests when an input state with a larger value of the EA, i.e. a greater degree of symmetry breaking, undergoes faster symmetry restoration than the one with a smaller value of the EA. Studying EA as a function of time, the QMPE is identified as a crossing of the EA curves for two states which are initialized at different degrees of symmetry-breaking [9]. This route to symmetry restoration can also be mapped via a state distance, such as the Frobenius distance [30],

which will be presented as a complementary approach to studying the QMPE. These studies performed on a quantum simulator not only allow us to investigate the QMPE in a non-integrable system but also provide insights into the robustness of the effect under realistic physical conditions. In contrast to other quantum versions of the Mpemba effect, which require an external reservoir to drive the system out of equilibrium [31–37], our studies involve an isolated quantum system undergoing a unitary evolution of a pure quantum state.

Our experiment marks the first observation of the QMPE in a many-body quantum system. We show that the presence of integrability-breaking interactions, and decoherence do not undermine its occurrence. The manuscript presents experimental studies of symmetry restoration of a tilted ferromagnet for various scenarios. At first, we present our findings for nearly unitary dy-

namics of a tilted ferromagnet; the experimental results show that the QMPE occurs for the interacting XY spin chain. We also explore the QMPE under (i) local disorders added to the interacting spin chain, and (ii) the scenario where tilted spins solely interact with the environmental noise, undergoing self-relaxation without being time evolved by a spin-spin interaction Hamiltonian. The former case reveals the QMPE for weak disorder strengths, however, when the disorder reaches a certain strength, it slows down the symmetry restoration, and subsequently weakens the presence of the QMPE. In the latter case, we do not find the QMPE.

II. RESULTS

We use a $N = 12$ qubit trapped-ion quantum simulator to study the QMPE. A linear string of calcium ions is held in a Paul trap and laser-cooled to the motional ground state. The spin states are encoded into two long-lived electronic states, $|S_{1/2}, m = 1/2\rangle$ and $|D_{5/2}, m = 5/2\rangle$ and manipulated by a narrow linewidth 729 nm laser. The experimental recipe for investigating the QMPE using randomized measurements is presented in Fig. 1a. The spin state is initialized to a ferromagnetic product state $|\downarrow\rangle^{\otimes N}$ and subsequently all spins are tilted by an angle θ using a laser beam that resonantly couples the two electronic states. The tilted state is then time-evolved (quenched) with the desired Hamiltonian, detailed below. After performing local random rotations U , site-selective projective measurements are performed on the time-evolved state. The observables related to symmetry-breaking and the state distance, i.e. the EA and the Frobenius distance for the subsystem of interest A , are estimated from the classical shadows. Further details about the experimental setup and estimators are provided in Methods IV A, IV B, IV C, and IV D.

A. Symmetry restoration with a long-range spin-spin interaction

The experimental data showing the QMPE are presented in Fig. 1b. We choose three tilt angles: $\theta = 0.2\pi$, $\theta = 0.33\pi$, and $\theta = 0.5\pi$ in increasing order of symmetry-breaking at $t = 0$ i.e. EA = 0.64, 1.12 and 1.3 for $N_A = 4$, respectively. The tilt angle dependence of the EA at initial time $t = 0$ is presented in the inset of Fig. 1b for subsystem size $N_A = 4$. The tilted ferromagnetic states are then quenched with a $U(1)$ symmetric Hamiltonian engineered in our experiment (see Methods IV A 1). The experimentally realized Hamiltonian is approximated with a power-law decaying XY interaction, given as,

$$H_{XY} = \sum_{i>j} \frac{J_0}{2|i-j|^\alpha} (\sigma_i^x \sigma_j^x + \sigma_i^y \sigma_j^y) , \quad (2)$$

where σ_i^a denote the Pauli matrices for $a = x, y$ at lattice site $i = 1 \dots N$. The realized interaction strength

and range in our setup are $J_0 \approx 560$ rad/s and $\alpha \approx 1$, respectively.

Under the time evolution with the XY Hamiltonian, the subsystem that is initialized to an asymmetric state is expected to attain the same symmetry of the Hamiltonian, i.e. the subsystem attains a rotation symmetry about the z axis (see Ref. [9]). The symmetry restoration for subsystems of size $N_A = 4$ is monitored by measuring the EA at various times in the experiment; see Fig. 1b. Here, the plotted EA is the average over all possible subsystems with size $N_A = 4$ from the central 6 lattice sites. We witness that the EA decreases and tends to zero for the three tilt angles, indicating that the subsystem state ρ_A evolves to a $U(1)$ symmetric state. The striking feature is that the EA decays faster for a state at $\theta = 0.5\pi$ than for states at $\theta = 0.33\pi$ and 0.2π ; i.e., in Fig. 1b the purple curve reaches zero before the green or the orange curve. Naively, one might assume that the state with the smallest initial EA would restore the symmetry the earliest. The observed crossing in EA curves confirms the QMPE. In Fig. 1b, the solid lines are numerical simulations carried out for the experimental conditions, with the inclusion of decoherence effects (see Methods IV E).

We further examine the robustness of the QMPE on the choice of subsystem A . For this, we evaluate the EA for various subsystems with fixed size $N_A = 4$ and plot the experimental results in Fig. 1c for tilt angles $\theta = 0.2\pi$ (green surface) and $\theta = 0.5\pi$ (purple surface). In the left panel, we display the results for subsystems that are connected. We have considered all connected subsystems of size $N_A = 4$ from one edge of the chain to the other edge. There are 9 of them which are $[1, 2, 3, 4], [2, 3, 4, 5], [3, 4, 5, 6], \dots$, here the integers denote ion indices. Notably, the subsystems that lie at the edges of the ion string display the crossing of the EA curves at later times than those from the middle of the chain (bulk region). This is attributed to the effect of boundaries, as the subsystems from the edge regions are accompanied by a lesser number of neighboring particles than the ones in the bulk. This effect becomes more pronounced for smaller system sizes, which we further discuss in Methods IV F. For the bulk region, the choice of the subsystem is extensively studied by considering all connected and disconnected subsystems from the bulk. In the right panel of Fig. 1c, we display the EA for the two tilt angles as a function of time and subsystem index. Here, we consider all possible subsystems, i.e. connected or disconnected subsystems, of size $N_A = 4$ forming 15 subsystems out of the central 6 ions. In contrast to the left panel of Fig. 1c, the crossing time of the EA for the two tilt angles does not depend upon the choice of the subsystem, which implies that the QMPE in the bulk region is robust against the choice of the subsystem.

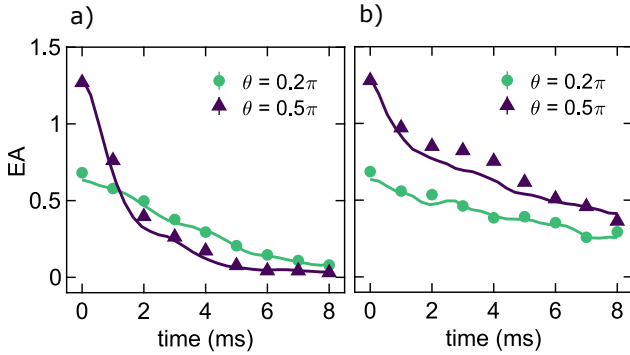


FIG. 2: The EA for tilted ferromagnetic states evolved under an XY interaction with disorders : a) In the presence of weak disorders, $h_i \in 6(0, J_0)$, we observe crossing in the EA for the two tilt angles as a function of interaction time, thus revealing the QMPE in the measurements. b) For the strong disorders, $h_i \in 14(0, J_0)$, QMPE is not visible in the measured data. The presented data are the averaged EAs for all 4 qubit subsystems out of the central 6 qubits. Solid curves denote theory and symbols are experimental data where the error bars are smaller than symbols

B. QMPE in the presence of disordered interactions

A central theme in modern research is to understand how localization alters the relaxation and thermalization dynamics in spin systems [38]. The versatility of our experimental setup enables us to study this interesting problem through the lens of the EA and the QMPE. On the experimental side, we add transverse disorder terms to our XY Hamiltonian, thus engineering a disorder Hamiltonian of the type,

$$H = \sum_{i>j} \frac{J_0}{2|i-j|^\alpha} (\sigma_i^x \sigma_j^x + \sigma_j^y \sigma_i^y) + \sum_i h_i \sigma_i^z. \quad (3)$$

The last term denotes static disorder terms realized in the experiment with site-dependent light shift laser beams [39]. The disorder fields are chosen randomly from a uniform distribution with disorder strengths $h_i \in w(0, J_0)$. The Hamiltonian (3) is $U(1)$ symmetric for each disorder realization and so can be exploited to study the QMPE. The tilted ferromagnetic states for two choices of tilt angles $\theta = 0.2\pi$ and 0.5π are evolved under this Hamiltonian. We consider weak ($w = 6$) and strong ($w = 14$) disorder configurations. The experiment is repeated for 5 disorder sets, for both the weak and strong disorder cases (see Methods IV G). In Fig. 2, we show the EA curves for $N_A = 4$, averaged over the 5 disorder realizations and all 15 subsystems of size 4 out of the central 6 ions. For the weak disorder, we observe the QMPE as the EA curves cross for the two tilt angles, indicating a faster drop of the EA for the input state with a larger

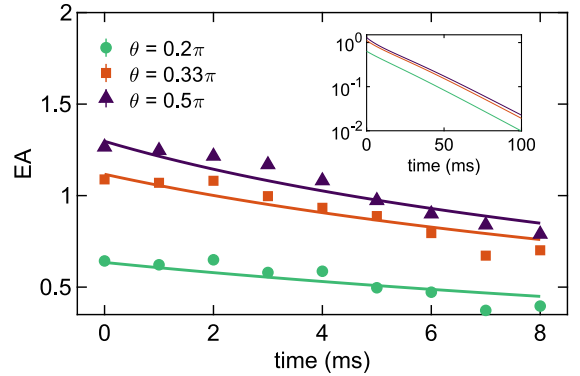


FIG. 3: The EA for pure dephasing evolution: Symmetry restoration under a pure dephasing evolution for three tilted ferromagnetic states; $\theta = 0.2\pi, 0.33\pi$, and 0.5π . Solid lines correspond to numerical simulations and data points are the experimental results averaged over 15 subsystems of $N_A = 4$ generated from the central 6 ions. Inset: simulation results are presented for late times. A reduction of the EA for all three tilt angles implies symmetry restoration, however, the QMPE is absent for the pure dephasing case since the EA curves do not cross.

EA at the beginning of the time evolution. Oppositely, for strong disorders, there is no crossing between the EA curves within the experimental time window. These results prove the robustness of the QMPE for weak disorders. On the other hand, the strong disorders localize the interactions to single sites thus preventing the subsystem thermalization in the accessible time window, suggesting that the subsystem thermalization led by entanglement is crucial for observing QMPE.

C. Relaxation of tilted ferromagnetic states under dephasing

So far we have studied the QMPE under near-unitary time evolution and investigated the QMPE for tilted ferromagnets evolved under the XY and XY+disorder Hamiltonian. Now we will explore a different scenario where the tilted ferromagnet evolves under a non-unitary evolution such as pure dephasing of the spins with the environmental noise. We turn the spin-spin interaction off and let the system freely evolve for time t . Due to the interaction with the fluctuating magnetic field in the laboratory and the phase noise of the laser beam (see Methods IV E), dephasing takes place in the experiment. Under this scenario, the initially asymmetric state is expected to symmetrize.

The experimental data are presented in Fig. 3 and the results are corroborated by numerical simulations. The measurement protocol is similar to the one presented in Fig. 1a except that the qubits are time-evolved under the ambient experimental noise. In this case, we observe the

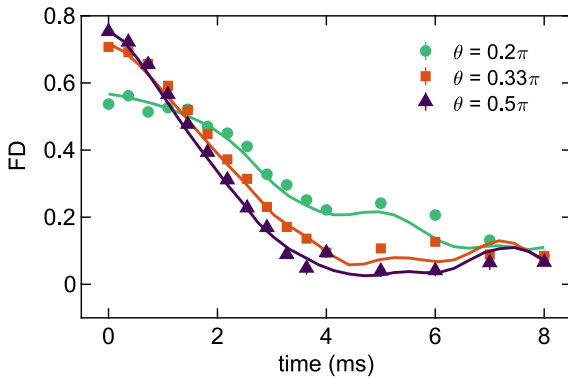


FIG. 4: Frobenius distances via classical shadows: the Frobenius distance (discussed in Methods IV D) between the experimental time-evolved state and the theoretical equilibrium state is shown for three tilt angles and $N_A = 4$. The state that is initially farthest from its equilibrium state attains the latter at the earliest time; confirming the QMPE in quantum simulations via Frobenius distance measures. Here also the solid lines are numerical simulations and the symbols are experimental data averaged over subsystems from the central region. Error bars are smaller than symbols.

restoration of symmetry, however, the crossing of the EA for various tilt angles, unlike in the previous cases, is not observed. The experimental data and numerical simulations, see inset, imply that pure dephasing evolution does not show the QMPE while undergoing symmetry restoration of initially asymmetric states. In Fig. 3, solid lines correspond to numerical simulations, which are carried out for the experimentally measured dephasing rates listed in Methods IV E.

D. Frobenius distance to observe QMPE

In a complementary approach, the route to symmetrization can also be probed by measuring the distance between two states — the experimental time-evolved state $\rho_A(t)$ and the diagonal ensemble ρ_A^{DE} [40] (more details in Methods IV D), which describes the averaged behavior of any observable at long times. The diagonal ensemble is a mixed state that is diagonal in the eigenbasis of the quenching XY Hamiltonian and, therefore, it is $U(1)$ symmetric. According to the eigenstate thermalization hypothesis, for large systems, this ensemble is equivalent to a Gibbs ensemble [18–20]. From the data obtained in the randomized measurements, we evaluate the Frobenius distance [30] between $\rho_A(t)$ and ρ_A^{DE} , see Methods IV D for definitions.

The results are presented in Fig. 4 for three tilt angles $\theta = 0.2\pi, 0.33\pi$ and 0.5π . From the present analysis, it is clear that the states which start farther away from the corresponding diagonal ensemble attain it earlier than

those which start comparably closer. As we see, the state at an angle 0.5π begins at the largest distance and relaxes to the diagonal ensemble the fastest. Such observation is the manifestation of the QMPE via Frobenius distance measurements.

Our findings constitute the first experimental evidence that the subsystem as a whole attains a stationary Gibbs ensemble. Although there exist previous experimental studies on the thermalization of isolated quantum systems [41–46], they predominantly focused on specific local observables.

III. SUMMARY AND OUTLOOK

In this manuscript, we have presented the first experimental demonstration of the QMPE. Notably, this phenomenon manifests itself at times much shorter than those relative to finite-size effects, such as revivals. This separation of time scales enables us to observe the QMPE distinctly in our experimental setup, comprising of a modest number of qubits ($N = 12$), even in presence of decoherence and disorder. Our investigation employs two distinct quantities, the entanglement asymmetry and the Frobenius distance, establishing that the QMPE is not specific to a particular observable. This versatility paves the way for further investigation employing a variety of theoretical and experimental tools.

Our focus in this study has been on a specific class of initial states — the tilted ferromagnets. However, our findings motivate future studies with other configurations to determine the experimental conditions for the occurrence of the QMPE in ergodic systems. While the role of entanglement in driving thermalization in isolated quantum systems is well understood, it will be important to elucidate the interplay between entanglement and quantum fluctuations for the observation of the QMPE in generic quantum systems. The measurement protocol presented in this work is easily applicable to other platforms with individual control and readout capabilities such as arrays of atoms in optical lattices, Rydberg systems, or superconducting qubits [17, 47–50]. This spotlights tantalizing opportunities for the experimental investigation of the QMPE, especially in higher dimensional systems where a richer phenomenology is expected due to the possibility of spontaneous symmetry breaking at finite temperatures. Our experimental findings may stimulate further theoretical investigations about the role played by dissipation and disorder in the dynamical restoration of symmetry. We believe that further studies on the QMPE will provide new protocols for faster preparation of thermal states (albeit at the subsystem level). Such states can then be used as input states for quantum simulation experiments. The experimentally accessible quantities discussed in the present manuscript, such as the EA and the Frobenius distance, will be valuable tools to assess the quality of the state preparation.

Note added:- While preparing our manuscript, we became aware of another experimental study of the Mpemba effect performed with a single trapped ion [51].

IV. METHODS

A. Experimental set-up

Here we use a trapped ion quantum simulator capable of storing and manipulating long ion strings for studying the QMPE. The experimental setup consists of a string of $N = 12$ calcium ions that is made to emulate a spin-1/2 chain with long-range interactions. Each qubit is labeled by basis vectors $s = (|\uparrow\rangle, |\downarrow\rangle) \equiv (|0\rangle, |1\rangle)$, which are encoded onto $|S_{1/2}, m = +1/2\rangle$ and $|D_{5/2}, m = +5/2\rangle$ electronic levels of a calcium ion. The power-law XY interaction expressed in Eq. (2) is engineered with the help of a global laser beam that interacts with ions' electronic and motional degrees of freedom from the transverse direction of the ion chain [15, 16]. Furthermore, the disordered Hamiltonian displayed in Eq. (3) is generated by shining a set of site-selective light shift beams along with the global entangling beam [39].

In our set-up, for the x and y global rotations, we use an elliptically shaped laser beam coupling to all ions simultaneously and driving the resonant optical transition between spin states. A tightly focused laser beam is used to perform local z rotations, by inducing an AC-Stark shift of variable strength on individual ions. Quantum projective measurements in the z basis are obtained via site-resolved fluorescence detection.

1. AC-Stark shift compensation during the spin-spin interaction

The trapped-ion platforms employ an Ising interaction when a bichromatic laser beam off-resonantly excites the motional red and blue sidebands of an ion chain [15]. In the case of symmetric detuning Δ of the bichromatic beam from the motional sidebands, an AC-Stark shift is present due to laser coupling to the ion's spectator levels. For example, in our setup, when the interaction is generated on the quadrupole transition of a calcium ion chain with a 729-nm laser beam, the off-resonant coupling to the dipole-allowed transitions gives an AC-Stark shift. We cancel this shift by adding a third frequency component to the laser beam, such that the light off-resonantly couples to the quadrupole transition and induces an AC-Stark shift that is of opposite sign but of equal strength compared to the dipole transitions.

The Ising interaction is then transformed into an XY interaction via asymmetrically driving the sidebands by $\Delta \pm \delta_c$. In the limit of δ_c being smaller than Δ and much larger than the spin-spin coupling strength J_0 , the

interaction Hamiltonian is written as [52],

$$H = \sum_{i>j} \frac{J_0}{2|i-j|^\alpha} (\sigma_i^x \sigma_j^x + \sigma_j^y \sigma_i^y) + \frac{\delta_c}{2\Delta} \sum_i B_i \sigma_i^z, \quad (4)$$

where an additional AC-Stark shift is induced that is proportional to δ_c . This term is often irrelevant when the input states are initialized in the eigenbasis of the σ_z operator. However, it is relevant when the input state is not the eigenstate of the σ_z operator, which is currently the case for $\theta \neq 0$. In the above equation, B_i depends upon the motional occupation number $\langle N_\ell \rangle$, site-dependent Rabi frequency Ω_i and mode dependent Lamb-Dicke parameter $\eta_{i,\ell}$; and it is expressed as

$$B_i = \Omega_i^2 \Delta \sum_\ell \frac{\eta_{i,\ell}^2}{\Delta_\ell^2} (\langle N_\ell \rangle + 1/2). \quad (5)$$

Here, Δ_ℓ is the laser detuning from the ℓ^{th} motional sideband. The shift can be different for each ion due to its dependence on the Lamb-Dicke parameter which is different for each ion. However, the major contribution comes from the center of mass mode, which is closest to the laser drive frequency, and it is eliminated by appropriately adjusting the intensity of the third frequency component of the laser beam.

B. Measurements

The measurement protocol is shown in Fig. 1a. We begin by preparing a ferromagnetic product state $\rho_{\text{ferro}} = (|\downarrow\rangle\langle\downarrow|)^{\otimes N} \equiv (|1\rangle\langle 1|)^{\otimes N}$. This state is $U(1)$ symmetric under rotations about the z axis. Next, we create initial states that explicitly break the $U(1)$ symmetry by rotating the state ρ_{ferro} about the $-y$ axis using the operator $R_{-y}(\theta) = \exp(i\theta S_y/2)$ with $S_y = \sum_i \sigma_i^y$. This allows us to create the symmetry breaking initial states $\rho(\theta)_{\text{init}} = R_{-y}(\theta)\rho_{\text{ferro}}R_y(\theta)$, where the tilt angle θ controls the extent of broken symmetry. This state is quenched with Hamiltonians of interest [Eqs. (2),(3)] for a duration t , leading to state $\rho(\theta, t)$ that is finally measured in random bases (detailed below). The measurements are performed for each tilt angle θ and time t independently, thus, hereon we drop the parenthesis in order to be concise.

The randomized measurement (RM) framework [28, 53] allows us to estimate desired quantities in a state-agnostic manner with a reduced measurement budget compared to the quantum state tomography [54]. This toolbox has allowed probing a large range of interesting quantum properties such as entanglement entropies [50, 55–57], negativities [58–60], bound entanglement [61, 62], quantum Fisher information [63, 64] and many-body quantum chaos [65]. The RM protocol requires applying unitaries $U = \bigotimes_{i=1}^N U_i$ to the time-evolved states, where each single qubit random rotation U_i is sampled from at least a 2-design. Then, the rotated

state $U\rho U^\dagger$ is projected in the z basis $|\mathbf{s}\rangle = |s_1, \dots, s_N\rangle$ with $s_i \in (0, 1)$. Note that in the experiment, we construct local random unitaries U_i by combining global x and y rotations with single qubit local z rotations whose angles are sampled randomly to obtain a set of unitaries from the circularly uniform ensemble (CUE) [66].

The protocol described above is repeated for N_U different random unitaries and recording N_M projective measurements for each random unitary. The experimental data thus obtained comprises of random unitaries $U^{(r)}$ and the respective recorded bitstring measurements $\mathbf{s}^{(r,m)} = (s_1^{(r,m)}, \dots, s_N^{(r,m)})$ with $r = 1, \dots, N_U$ and $m = 1, \dots, N_M$ that are stored in a classical device for post-processing. From the collected RM dataset, we can construct operators known as *classical shadows* of the prepared state ρ in the post-processing stage. This operator restricted to a given subsystem of interest A can be defined as [28, 29]

$$\hat{\rho}_A^{(r,m)} = \bigotimes_{i \in A} 3 U_i^{(r)\dagger} |s_i^{(r,m)}\rangle\langle s_i^{(r,m)}| U_i^{(r)} - \mathbb{I}_2. \quad (6)$$

These classical shadows form an unbiased estimator of the underlying density matrix of interest, that is, the average over the applied unitaries and the measurement outcomes gives $\mathbb{E}[\hat{\rho}_A^{(r,m)}] = \rho_A$.

C. Estimation of EA

The shadows defined in Eq. (6) can be used to extract arbitrary multi-copy functionals of the form $f_n = \text{Tr}(O_A^{(n)} \rho_A^{\otimes n})$ defined on the subsystem of interest using the U-statistics estimator [67]:

$$\hat{f}_n = \frac{1}{n!} \binom{N_U}{n}^{-1} \sum_{r_1 \neq \dots \neq r_n} \text{Tr} \left(O_A^{(n)} \bigotimes_{j=1}^n \hat{\rho}_A^{(r_j)} \right), \quad (7)$$

which is an unbiased estimator of f_n , i.e. $\mathbb{E}[\hat{f}_n] = f_n$. We also define here the classical shadow $\hat{\rho}_A^{(r)} = \mathbb{E}_{N_M}[\hat{\rho}_A^{(r,m)}]$, constructed by averaging over N_M measured bitstrings for an applied unitary $U^{(r)}$. Additionally, the classical shadow formalism allows one to estimate interesting symmetry-resolved quantum properties of the underlying quantum state as shown in the Refs. [60, 68, 69]. In this work, in order to obtain an estimator $\widehat{\text{EA}}$ of Eq. (1) from the RM dataset, we construct unbiased estimators of each of the individual trace moment term in Eq. (1) following Refs. [28, 68]. This writes as,

$$\widehat{\text{EA}} = \log \frac{\sum_{r_1 \neq r_2} \text{Tr} \left(\hat{\rho}_A^{(r_1)} \hat{\rho}_A^{(r_2)} \right)}{\sum_{r_1 \neq r_2} \text{Tr} \left(\hat{\rho}_{A,Q}^{(r_1)} \hat{\rho}_{A,Q}^{(r_2)} \right)}, \quad (8)$$

where $\hat{\rho}_{A,Q}^{(r)}$ is the shadow for the symmetrized counterpart of $\hat{\rho}_A^{(r)}$ given by $\hat{\rho}_{A,Q}^{(r)} = \sum_{q \in \mathbb{Z}} \Pi_q \hat{\rho}_A^{(r)} \Pi_q$ that satisfies

$\mathbb{E}[\hat{\rho}_{A,Q}^{(r)}] = \rho_{A,Q}$. Rigorous performance analysis of statistical errors from a finite number of experimental runs $N_U \times N_M$ in the estimation of such trace moments have been studied in various prior works [29, 59, 60, 63].

In the main text, the experiment for quenching with XY Hamiltonian (Fig. 1b) is done with $N_U = 500$ and $N_M = 30$ projective measurements for each random unitary. The experiment in the presence of disorder (results in Fig. 2) and pure dephasing (results in Fig. 3) is done with $N_U = 300$ and $N_M = 30$ projective measurements for each random unitary.

D. Frobenius distance

For generic large quantum systems evolving unitarily, the reduced density matrix describing the subsystem A is expected to relax, at long times, to a Gibbs distribution [18–20]. The eigenstate thermalization hypothesis [18, 19] predicts that such thermal state is equivalent to the reduced density matrix of the diagonal ensemble [20, 40]. The diagonal ensemble is obtained by projecting the initial density matrix onto the eigenbasis $\{|E_k\rangle\}$ of the quenching Hamiltonian, that is

$$\rho^{\text{DE}}(\theta) = \sum_k \langle E_k | \rho(\theta, t=0) | E_k \rangle |E_k\rangle\langle E_k|, \quad (9)$$

where $\rho(\theta, t=0)$ is the initial state. The partial trace of this state $\rho_A^{\text{DE}}(\theta) = \text{Tr}_{\bar{A}}(\rho^{\text{DE}}(\theta))$ gives the averaged behavior of local operators at long times. For each tilt angle θ , we are interested in the Frobenius distance between the post-quench state of subsystem A at a given time and the corresponding diagonal ensemble i.e., the distance $\text{FD}[\rho_A(\theta, t), \rho_A^{\text{DE}}(\theta)]$, defined as [30],

$$\text{FD}(\rho_A, \rho_A^{\text{DE}}) = \sqrt{1 - \frac{2\text{Tr}[\rho_A \rho_A^{\text{DE}}]}{\text{Tr}[\rho_A^2 + (\rho_A^{\text{DE}})^2]}}, \quad (10)$$

where we have dropped the angle θ and time t for brevity. In the main text, we utilized this distance to analyze the thermalization of the reduced density matrix after the XY Hamiltonian quench (see Fig. 4).

The rich RM dataset obtained using the protocol described above equally allows us to extract the Frobenius distance. Namely, we can estimate unbiased estimators of all the individual terms in the expression of the Frobenius distance (10) from the *same* dataset collected during the experimental execution. Thus the explicit expression of the estimator $\widehat{\text{FD}}$ of the Frobenius distance can be written as

$$\widehat{\text{FD}} = \left(1 - \frac{\frac{2}{N_U} \sum_{r_1} \text{Tr}[\hat{\rho}_A^{(r_1)} \rho_A^{\text{DE}}]}{\beta^{-1} \sum_{r_1 \neq r_2} \text{Tr}[\hat{\rho}_A^{(r_1)} \hat{\rho}_A^{(r_2)}] + \text{Tr}[(\rho_A^{\text{DE}})^2]} \right)^{1/2} \quad (11)$$

with $\beta = N_U(N_U - 1)$.

E. Experimental noise

The dominant decoherence effect in our experiment is that of dephasing noise, an unwanted noise that randomly rotates the spin vector along the z axis. In our system, the dephasing is a combination of laser phase noise/frequency noise and magnetic-field noise. We measure the overall effect of noise by performing Ramsey measurements for entangling interaction, disorder, and pure dephasing cases. For the XY quenches, the measured coherence time is $T_{\text{coh}} \sim 16$ ms. The coherence time here is measured such that we could account for laser phase noise, magnetic field noise, and fluctuating AC-Stark shift due to thermal occupation of the motional modes. Specifically, the measured coherence time without turning on the quench beam is $T_{\text{coh}} \sim 45$ ms.

A shorter coherence time in the case of entangling interactions can be explained by considering the thermal occupation of the motional modes. While writing this manuscript we became aware of this issue and carried out some detailed experimental and numerical studies beyond the scope of the present manuscript and verified that the drop in the coherence time is indeed due to this effect. Its impact can be understood from the second term of Eq. (4). The AC-Stark shift in this case linearly follows the phonon number, thus imperfect ground-state cooling or motional heating increases the dephasing rates in the system. To improve this coherence, we are currently working on implementing better ground-state cooling methods in our system and designing a new ion trap to reduce the motional heating of the ion string.

In the disorder studies, we use a spin-echo sequence to mitigate slow drifts in the experimental parameters. To do so, an echo pulse, i.e. a π rotation about the x axis in the middle of the time evolution is applied. The coherence time measured is $T_{\text{coh}} \sim 27(2)$ ms for strong disorders and $T_{\text{coh}} \sim 27(4)$ ms for weak disorders. In the case of pure dephasing, where the prepared state is left to evolve under dephasing noise without interactions, we observe slow detrimental noise components affect the quality of randomized measurements. To overcome this, we again use a spin-echo sequence. The measured coherence time is $T_{\text{coh}} \sim 45(4)$ ms.

In the numerical simulation shown in the results, we have considered a global dephasing mechanism with experimentally measured rates. The corresponding jump operator is $\sqrt{\Gamma} \sum_i \sigma_i^z$, where $\Gamma = 1/(2T_{\text{coh}})$. The spontaneous decay rate and depolarization noise rate reported elsewhere [12] are negligible compared to these rates and hence they are not the leading error sources for the current studies. To counteract slow drifts of the experimental parameters, the system is calibrated every few minutes for changes in clock transition, laser pulse area fluctuation, and shift in the ion position.

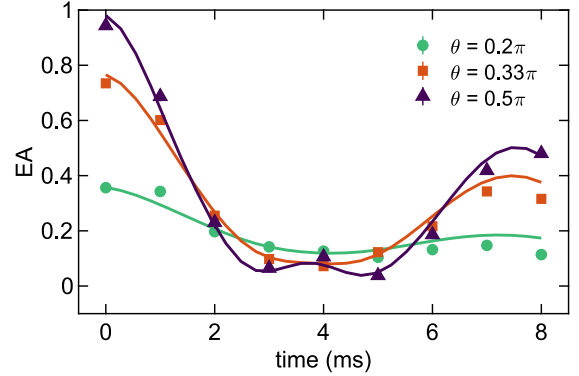


FIG. 5: **EA in a 4-qubit system:** EA, averaged over all possible subsystems, is plotted for $N_A = 2$ and three tilt angles. The subsystem restores the symmetry and QMPE is observed. However, a revival of the EA is seen due to the finite-size effects.

F. Finite size effects: 4-qubit experiment

To explore the finite-size effects within the experiment's coherence time, we measure the EA for a 4-qubit system and present the results of the EA for $N_A = 2$ subsystems. Data are plotted in Fig. 5. Here, symbols correspond to experimental data, and solid lines correspond to numerical simulations in the presence of global dephasing. It is important to note that QMPE is present even for the smallest system that we probed in the experiment. However, a revival of the EA is observed due to finite-size effects. In fact, in this case, thermalization is hindered and thus the subsystem oscillates between the asymmetric and symmetric states.

G. Implementation of disorder in the experiment

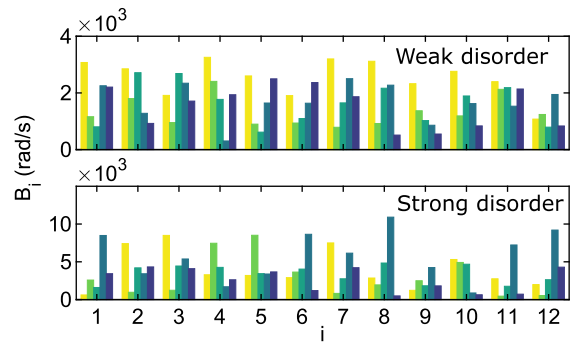


FIG. 6: **Experimentally measured disorders:** Measured disorders versus ion index for strong and weak disorder realizations. Different colors correspond to 5 sets of different realizations of disorders.

In our experimental system, the disorders are realized by shining multiple laser beams generated by an acousto-optic deflector (AOD) on individual ions. The AOD deflects multiple laser beams designated to individual ions with the desired light intensity such that site-specific AC-Stark shifts are induced. We sample 5 sets of weak and strong disorders randomly chosen from a uniform distribution function and apply them to the ion string. In Fig. 6, we show measured disorders for both the strong and weak disorder cases.

ACKNOWLEDGMENTS

The experimental team (JF, FK, MKJ, CR, RB) would like to acknowledge funding from the Institut für Quanteninformation GmbH and European Union's Horizon 2020 research and innovation programme under grant agreement No 101113690 (PASQuanS2.1). LKJ, BV and PZ acknowledge funding from the Austrian Science Foundation (FWF, P 32597 N). LKJ acknowledges financial support from the PNRR MUR project PE0000023-NQST, and HPC and supercomputer facilities of the University of Innsbruck, where most of the numerical simulations were carried out. PZ acknowledges the funding from the Simons Collaboration on Ultra-Quantum Matter, which is a grant from the Simons Foundation (651440). PC and FA are supported by ERC under Consolidator Grant number 771536 (NEMO). SM acknowledges the support from the Caltech Institute for Quantum Information and Matter and the Walter Burke Insti-

tute for Theoretical Physics at Caltech. Work in Grenoble is funded by the French National Research Agency via the JCJC project QRand (ANR-20-CE47-0005), and via the research programs Plan France 2030 EPIQ (ANR-22-PETQ-0007), QUBITAF (ANR-22-PETQ-0004) and HQI (ANR-22-PNCQ-0002). A.R. acknowledges support by Laboratoire d'excellence LANEF in Grenoble (ANR-10-LABX-51-01) and from the Grenoble Nanoscience Foundation. In numerical simulations, we have used the quantum toolbox QuTiP [70].

AUTHOR CONTRIBUTION

JF, MJ, FK, RB, and CFR contributed to the experimental setup. JF and MJ performed the experimental measurements. LKJ and MJ performed the data analysis and numerical simulations with inputs from AR. The theory idea was conceived by FA, SM, and PC. Quantum protocol and data processing methods were developed by AR, BV, PZ, and LKJ. Manuscript writing was carried out by MJ, LKJ, AR, SM, FA, and PC following the inputs from all the authors. All authors contributed to the discussion of the results.

Competing interest— The authors declare that they have no competing interests.

Data availability statement— All data needed to evaluate the conclusions in the paper are present in the paper and/or the Supplementary Materials. The raw and analyzed data will be uploaded to the Zenodo repository on this link doi: 10.5281/zenodo.10390690.

[1] E. B. Mpemba and D. G. Osborne, Cool?, *Phys. Educ.* **4**, 312 (1969).

[2] A. Lasanta, F. Vega Reyes, A. Prados, and A. Santos, When the Hotter Cools More Quickly: Mpemba Effect in Granular Fluids, *Phys. Rev. Lett.* **119**, 148001 (2017).

[3] Z. Lu and O. Raz, Nonequilibrium thermodynamics of the Markovian Mpemba effect and its inverse, *PNAS* **114**, 5083 (2017).

[4] I. Klich, O. Raz, O. Hirschberg, and M. Vucelja, Mpemba Index and Anomalous Relaxation, *Phys. Rev. X* **9**, 021060 (2019).

[5] A. Kumar and J. Bechhoefer, Exponentially faster cooling in a colloidal system, *Nature* **584**, 64 (2020).

[6] J. Bechhoefer, A. Kumar, and R. Chétrite, A fresh understanding of the Mpemba effect, *Nat. Rev. Phys.* **3**, 534 (2021).

[7] A. Kumar, R. Chétrite, and J. Bechhoefer, Anomalous heating in a colloidal system, *PNAS* **119**, e2118484119 (2022).

[8] G. Teza, R. Yaacoby, and O. Raz, Relaxation Shortcuts through Boundary Coupling, *Phys. Rev. Lett.* **131**, 17101 (2023).

[9] F. Ares, S. Murciano, and P. Calabrese, Entanglement asymmetry as a probe of symmetry breaking, *Nat. Commun.* **14**, 2036 (2023).

[10] C. Rylands, K. Klobas, F. Ares, P. Calabrese, S. Murciano, and B. Bertini, Microscopic origin of the quantum Mpemba effect in integrable systems, [arXiv:2310.04419](https://arxiv.org/abs/2310.04419) (2023).

[11] J. Zhang, G. Pagano, P. W. Hess, A. Kyprianidis, P. Becker, H. Kaplan, A. V. Gorshkov, Z.-X. Gong, and C. Monroe, Observation of a many-body dynamical phase transition with a 53-qubit quantum simulator, *Nature* **551**, 601 (2017).

[12] M. K. Joshi, F. Kranzl, A. Schuckert, I. Lovas, C. Maier, R. Blatt, M. Knap, and C. F. Roos, Observing emergent hydrodynamics in a long-range quantum magnet, *Science* **376**, 720 (2022).

[13] P. Scholl, M. Schuler, H. J. Williams, A. A. Eberharter, D. Barredo, K.-N. Schymik, V. Lienhard, L.-P. Henry, T. C. Lang, T. Lahaye, A. M. Läuchli, and A. Browaeys, Quantum simulation of 2D antiferromagnets with hundreds of Rydberg atoms, *Nature* **595**, 233 (2021).

[14] J. W. Britton, B. C. Sawyer, A. C. Keith, C.-C. J. Wang, J. K. Freericks, H. Uys, M. J. Biercuk, and J. J. Bollinger, Engineered two-dimensional Ising interactions in a trapped-ion quantum simulator with hundreds of spins, *Nature* **484**, 489 (2012).

[15] D. Porras and J. I. Cirac, Effective Quantum Spin Systems with Trapped Ions, *Phys. Rev. Lett.* **92**, 207901

(2004).

[16] P. Jurcevic, B. P. Lanyon, P. Hauke, C. Hempel, P. Zoller, R. Blatt, and C. F. Roos, Quasiparticle engineering and entanglement propagation in a quantum many-body system, *Nature* **511**, 202 (2014).

[17] C. Monroe, W. C. Campbell, L.-M. Duan, Z.-X. Gong, A. V. Gorshkov, P. W. Hess, R. Islam, K. Kim, N. M. Linke, G. Pagano, P. Richerme, C. Senko, and N. Y. Yao, Programmable quantum simulations of spin systems with trapped ions, *Rev. Mod. Phys.* **93**, 025001 (2021).

[18] J. M. Deutsch, Quantum statistical mechanics in a closed system, *Phys. Rev. A* **43**, 2046 (1991).

[19] M. Srednicki, Chaos and quantum thermalization, *Phys. Rev. E* **50**, 888 (1994).

[20] M. Rigol, V. Dunjko, and M. Olshanii, Thermalization and its mechanism for generic isolated quantum systems, *Nature* **584**, 64 (2020).

[21] P. C. Hohenberg, Existence of long-range order in one and two dimensions, *Phys. Rev.* **158**, 383 (1967).

[22] N. D. Mermin and H. Wagner, Absence of ferromagnetism or antiferromagnetism in one- or two-dimensional isotropic heisenberg models, *Phys. Rev. Lett.* **17**, 1133 (1966).

[23] B. J. J. Khor, D. M. Kürkçüoglu, T. J. Hobbs, G. N. Perdue, and I. Klich, Confinement and Kink Entanglement Asymmetry on a Quantum Ising Chain, [arXiv:2312.08601](https://arxiv.org/abs/2312.08601) (2023).

[24] L. Capizzi and M. Mazzoni, Entanglement asymmetry in the ordered phase of many-body systems: the Ising Field Theory, [arXiv:2307.12127](https://arxiv.org/abs/2307.12127) (2023).

[25] M. Chen and H.-H. Chen, Entanglement asymmetry in 1+1-dimensional Conformal Field Theories, [arXiv:2310.15480](https://arxiv.org/abs/2310.15480) (2023).

[26] L. Capizzi and V. Vitale, A universal formula for the entanglement asymmetry of matrix product states, [arXiv:2310.01962](https://arxiv.org/abs/2310.01962) (2023).

[27] F. Ares, S. Murciano, L. Piroli, and P. Calabrese, An entanglement asymmetry study of black hole radiation, [arXiv:2311.12683](https://arxiv.org/abs/2311.12683) (2023).

[28] A. Elben, S. T. Flammia, H.-Y. Huang, R. Kueng, J. Preskill, B. Vermersch, and P. Zoller, The randomized measurement toolbox, *Nat. Rev. Phys.* **5**, 9 (2023).

[29] H.-Y. Huang, R. Kueng, and J. Preskill, Predicting many properties of a quantum system from very few measurements, *Nat. Phys.* **16**, 1050 (2020).

[30] M. Fagotti and F. H. L. Essler, Reduced density matrix after a quantum quench, *Phys. Rev. B* **87**, 245107 (2013).

[31] A. Nava and M. Fabrizio, Lindblad dissipative dynamics in the presence of phase coexistence, *Phys. Rev. B* **100**, 125102 (2019).

[32] F. Carollo, A. Lasanta, and I. Lesanovsky, Exponentially Accelerated Approach to Stationarity in Markovian Open Quantum Systems through the Mpemba Effect, *Phys. Rev. Lett.* **127**, 060401 (2021).

[33] S. K. Manikandan, Equidistant quenches in few-level quantum systems, *Phys. Rev. Res.* **3**, 043108 (2021).

[34] S. Kochsieck, F. Carollo, and I. Lesanovsky, Accelerating the approach of dissipative quantum spin systems towards stationarity through global spin rotations, *Phys. Rev. A* **106**, 012207 (2022).

[35] F. Ivander, N. Anto-Sztrikacs, and D. Segal, Hyperacceleration of quantum thermalization dynamics by bypassing long-lived coherences: An analytical treatment, *Phys. Rev. E* **108**, 014130 (2023).

[36] A. K. Chatterjee, S. Takada, and H. Hayakawa, Quantum Mpemba Effect in a Quantum Dot with Reservoirs, *Phys. Rev. Lett.* **131**, 080402 (2023).

[37] A. K. Chatterjee, S. Takada, and H. Hayakawa, Multiple quantum Mpemba effect: exceptional points and oscillations, [arXiv:2311.01347](https://arxiv.org/abs/2311.01347) (2023).

[38] D. A. Abanin, E. Altman, I. Bloch, and M. Serbyn, Many-body localization, thermalization, and entanglement, *Rev. Mod. Phys.* **91**, 021001 (2019).

[39] C. Maier, T. Brydges, P. Jurcevic, N. Trautmann, C. Hempel, B. P. Lanyon, P. Hauke, R. Blatt, and C. F. Roos, Environment-Assisted Quantum Transport in a 10-qubit Network, *Phys. Rev. Lett.* **122**, 050501 (2019).

[40] M. Rigol, V. Dunjko, V. Yurovsky, and M. Olshanii, Relaxation in a Completely Integrable Many-Body Quantum System: An Ab Initio Study of the Dynamics of the Highly Excited States of 1D Lattice Hard-Core Bosons, *Phys. Rev. Lett.* **98**, 050405 (2007).

[41] M. Gring, M. Kuhnert, T. Langen, T. Kitagawa, B. Rauer, M. Schreitl, I. Mazets, D. A. Smith, E. Demler, and J. Schmiedmayer, Relaxation and Prethermalization in an Isolated Quantum System, *Science* **337**, 1318 (2012).

[42] S. Trotzky, Y.-A. Chen, A. Flesch, I. P. McCulloch, U. Schollwöck, J. Eisert, and I. Bloch, Probing the relaxation towards equilibrium in an isolated strongly correlated one-dimensional Bose gas, *Nat. Phys.* **8**, 325 (2012).

[43] A. M. Kaufman, M. E. Tai, A. Lukin, M. Rispoli, R. Schittko, P. M. Preiss, and M. Greiner, Quantum thermalization through entanglement in an isolated many-body system, *Science* **353**, 794 (2016).

[44] C. Neill, P. Roushan, M. Fang, Y. Chen, M. Kolodrubetz, Z. Chen, A. Megrant, R. Barends, B. Campbell, B. Chiaro, A. Dunsworth, E. Jeffrey, J. Kelly, J. Mutus, P. J. J. O’Malley, C. Quintana, D. Sank, A. Vainsencher, J. Wenner, T. C. White, A. Polkovnikov, and J. M. Martinis, Ergodic dynamics and thermalization in an isolated quantum system, *Nat. Phys.* **12**, 1037 (2016).

[45] M. Ueda, Quantum equilibration, thermalization and prethermalization in ultracold atoms, *Nat. Rev. Phys.* **2**, 669 (2020).

[46] Z.-Y. Zhou, G.-X. Su, J. C. Halimeh, R. Ott, H. Sun, P. Hauke, B. Yang, Z.-S. Yuan, J. Berges, and J.-W. Pan, Thermalization dynamics of a gauge theory on a quantum simulator, *Science* **377**, 311 (2022).

[47] A. J. Daley, I. Bloch, C. Kokail, S. Flannigan, N. Pearson, M. Troyer, and P. Zoller, Practical quantum advantage in quantum simulation, *Nature* **607**, 667 (2022).

[48] I. Bloch, J. Dalibard, and W. Zwerger, Many-body physics with ultracold gases, *Rev. Mod. Phys.* **80**, 885 (2008).

[49] S. J. Evered, D. Bluvstein, M. Kalinowski, S. Ebadi, T. Manovitz, H. Zhou, S. H. Li, A. A. Geim, T. T. Wang, N. Maskara, H. Levine, G. Semeghini, M. Greiner, V. Vuletić, and M. D. Lukin, High-fidelity parallel entangling gates on a neutral-atom quantum computer, *Nature* **622**, 268 (2023).

[50] J. C. Hoke, M. Ippoliti, E. Rosenberg, et al., Measurement-induced entanglement and teleportation on a noisy quantum processor, *Nature* **622**, 481 (2023).

[51] S. A. Shapira, Y. Shapira, J. Markov, G. Teza, N. Akerman, O. Raz, and R. Ozeri, The mpemba effect demonstrated on a single trapped ion qubit, To appear in the same Arxiv posting.

[52] I. Arrazola, J. S. Pedernales, L. Lamata, and E. Solano, Digital-Analog Quantum Simulation of Spin Models in Trapped Ions, *Sci. Rep.* **6**, 30534 (2016).

[53] P. Cieśliński, S. Imai, J. Dziewior, O. Gühne, L. Knips, W. Laskowski, J. Meinecke, T. Paterek, and T. Vértesi, Analysing quantum systems with randomised measurements, [arXiv:2307.01251](https://arxiv.org/abs/2307.01251) (2023).

[54] J. Haah, A. W. Harrow, Z. Ji, X. Wu, and N. Yu, Sample-optimal tomography of quantum states, *IEEE Trans. Inf. Theory* **63**, 5628 (2017).

[55] T. Brydges, A. Elben, P. Jurcevic, B. Vermersch, C. Maier, B. P. Lanyon, P. Zoller, R. Blatt, and C. F. Roos, Probing Rényi entanglement entropy via randomized measurements, *Science* **364**, 260 (2019).

[56] A. Rath, R. van Bijnen, A. Elben, P. Zoller, and B. Vermersch, Importance sampling of randomized measurements for probing entanglement, *Phys. Rev. Lett.* **127**, 200503 (2021).

[57] K. J. Satzinger, Y.-J. Liu, A. Smith, C. Knapp, et al., Realizing topologically ordered states on a quantum processor, *Science* **374**, 1237 (2021).

[58] Y. Zhou, P. Zeng, and Z. Liu, Single-Copies Estimation of Entanglement Negativity, *Phys. Rev. Lett.* **125**, 200502 (2020).

[59] A. Elben, R. Kueng, H.-Y. R. Huang, R. van Bijnen, C. Kokail, M. Dalmonte, P. Calabrese, B. Kraus, J. Preskill, P. Zoller, and B. Vermersch, Mixed-State Entanglement from Local Randomized Measurements, *Phys. Rev. Lett.* **125**, 200501 (2020).

[60] A. Neven, J. Carrasco, V. Vitale, C. Kokail, A. Elben, M. Dalmonte, P. Calabrese, P. Zoller, B. Vermersch, R. Kueng, and B. Kraus, Symmetry-resolved entanglement detection using partial transpose moments, *npj Quantum Inf.* **7**, 152 (2021).

[61] S. Imai, N. Wyderka, A. Ketterer, and O. Gühne, Bound entanglement from randomized measurements, *Phys. Rev. Lett.* **126**, 150501 (2021).

[62] C. Zhang, Y.-Y. Zhao, N. Wyderka, S. Imai, A. Ketterer, N.-N. Wang, K. Xu, K. Li, B.-H. Liu, Y.-F. Huang, C.-F. Li, G.-C. Guo, and O. Gühne, Experimental verification of bound and multiparticle entanglement with the randomized measurement toolbox, [arXiv:2307.04382](https://arxiv.org/abs/2307.04382) (2023).

[63] A. Rath, C. Branciard, A. Minguetti, and B. Vermersch, Quantum Fisher Information from Randomized Measurements, *Phys. Rev. Lett.* **127**, 260501 (2021).

[64] V. Vitale, A. Rath, P. Jurcevic, A. Elben, C. Branciard, and B. Vermersch, Estimation of the Quantum Fisher Information on a quantum processor, [arXiv:2307.16882](https://arxiv.org/abs/2307.16882) (2023).

[65] L. K. Joshi, A. Elben, A. Vikram, B. Vermersch, V. Galitski, and P. Zoller, Probing many-body quantum chaos with quantum simulators, *Phys. Rev. X* **12**, 011018 (2022).

[66] F. Mezzadri, How to generate random matrices from the classical compact groups, *Notices Am. Math. Soc.* **54**, 592 (2007).

[67] W. Hoeffding, A class of statistics with asymptotically normal distribution, *Ann. Math. Statist.* **19**, 293 (1948).

[68] V. Vitale, A. Elben, R. Kueng, A. Neven, J. Carrasco, B. Kraus, P. Zoller, P. Calabrese, B. Vermersch, and M. Dalmonte, Symmetry-resolved dynamical purification in synthetic quantum matter, *SciPost Phys.* **12**, 1 (2022).

[69] A. Rath, V. Vitale, S. Murciano, M. Votto, J. Dubail, R. Kueng, C. Branciard, P. Calabrese, and B. Vermersch, Entanglement Barrier and its Symmetry Resolution: Theory and Experimental Observation, *PRX Quantum* **4**, 010318 (2023).

[70] J. Johansson, P. Nation, and F. Nori, Qutip 2: A python framework for the dynamics of open quantum systems, *Computer Physics Communications* **184**, 1234 (2013).